



LAWRENCE
LIVERMORE
NATIONAL
LABORATORY

The Influence of Cooling Rate on Condensation of Iron, Aluminum, and Uranium oxides

B. Koroglu, M. Finko, S. Foster, D. Lucas, D. McGuffin,
C. Saggese, S. Wagnon, D. Weisz, J. Crowhurst, H.
Radousky, D. Weisz, D. Curreli, K. Knight

February 25, 2021

Journal of Aerosol Science

Disclaimer

This document was prepared as an account of work sponsored by an agency of the United States government. Neither the United States government nor Lawrence Livermore National Security, LLC, nor any of their employees makes any warranty, expressed or implied, or assumes any legal liability or responsibility for the accuracy, completeness, or usefulness of any information, apparatus, product, or process disclosed, or represents that its use would not infringe privately owned rights. Reference herein to any specific commercial product, process, or service by trade name, trademark, manufacturer, or otherwise does not necessarily constitute or imply its endorsement, recommendation, or favoring by the United States government or Lawrence Livermore National Security, LLC. The views and opinions of authors expressed herein do not necessarily state or reflect those of the United States government or Lawrence Livermore National Security, LLC, and shall not be used for advertising or product endorsement purposes.

The Influence of Cooling Rate on Condensation of Iron, Aluminum, and Uranium Oxide Nanoparticles

LLNL-JRNL-819911

This work was performed under the auspices of the U.S. Department of Energy by Lawrence Livermore National Laboratory under Contract DE-AC52-07NA27344.

Authors: Batikan Koroglu^{*1}, Mikhail Finko^{1,2}, Chiara Saggese¹, Scott Wagnon¹, Samuel Foster¹, Dana McGuffin¹, Don Lucas¹, Tim P. Rose¹, Jonathan C. Crowhurst¹, David G. Weisz¹, Harry B. Radousky¹, Davide Curreli², Kim B. Knight¹

Affiliations:

¹Physical and Life Sciences, Lawrence Livermore National Laboratory, Livermore, CA, 94550

²Nuclear Plasma and Radiological Engineering, College of Engineering, University of Illinois at Urbana-Champaign, Urbana, IL, 61801

***Corresponding Author:** koroglu1@llnl.gov

Abstract

Fundamental observations of particle size distributions are needed to develop models that predict the fate and transport of radioactive materials in the atmosphere following a nuclear incident. The extent of material transport is influenced by the time scales of particle formation processes (e.g., condensation, coagulation). In this study, we investigated the influence of cooling time scales on size distributions of uranium, aluminum, and iron oxide particles that are synthesized separately under identical run conditions inside the controlled environment of an argon plasma flow reactor. Two distinct temperature distributions are imposed along the flow reactor by varying the argon flow rate downstream of the plasma torch. The vaporized reactants of uranium, aluminum, and iron are cooled from about 5000 K to 1000 K before they are collected on silicon wafers for *ex situ* scanning electron microscope analysis. The microscope images show that the sizes of largest aluminum and iron oxide particles heavily depend on the cooling time scales, whereas significant size variations with cooling rate is not observed for uranium oxide particles. In addition, the size distribution of aluminum oxide particles exhibits the broadest range among all three metal oxides studied. We performed simulations of particle size distributions using a kinetic model that couples gas phase oxidation chemistry with particle formation processes, including nucleation, condensation, and coagulation. The model results demonstrate the strong sensitivity of particle size distribution to different cooling histories (i.e., temperature vs residence time) along the flow reactor. The kinetic model also helps identify directions for future research to improve the predictions.

1. INTRODUCTION

In the aftermath of a nuclear incident (e.g., explosion (Freiling, 1961) or reactor accident (Ochiai et al., 2018)) chemical speciation, nucleation, and condensation behaviors drive the timing and activity distributions of radionuclides in resulting materials. Understanding how these processes affect the resulting size distributions of particles is essential to predicting the transport of radioactive aerosol particles that form and disperse in the atmosphere. The extent of the material transport is largely determined by the size distributions of micro- and nano-scale materials that are generally enriched in volatile constituents. However, there are exceptions to this pattern due to anomalous fractionation behaviors that cause the refractory metal oxides to appear together with their volatile counterparts. For example, the fractionation patterns of radionuclides in nuclear fallout debris become more difficult to predict in low-yield events and this behavior is generally attributed to the increase in the rate of cooling of the nuclear fireball (Moody et al., 2015; S. Glasstone and P. J. Dolan, 1977). Fundamental observations of particle size distributions under different time scales of cooling from vapor phase are needed to understand the relative importance of speciation, nucleation, and condensation processes. In the present study, we have investigated how cooling rates affect particle characteristics by performing controlled vapor-phase condensation experiments using refractory materials. The goal is to evaluate how the size distributions of particles respond to changes in cooling time scales.

Following a nuclear explosion, vaporized material can form new particles through gas-to-particle nucleation (Oxtoby, 1992). Vaporized material can also condense on existing particles at a rate dependent on the sizes of the particles and the saturation vapor pressure of the condensing material (Loyalka, 1983; Sitarski & Nowakowski, 1979) with refractory materials condensing faster than semi-refractory and volatile materials. Vapor that condenses on to existing particles is not available to nucleate new particles, and vice versa. These processes are in competition with each other and affect the final size distribution of particles. The relative importance of nucleation, condensation, and cluster-cluster agglomeration for general gas-to-particle conversion processes were studied in the past for various chemical species (Gelbard & Seinfeld, 1979; Nanjaiah et al., 2020; Savel'ev & Starik, 2018). However, few data exist to describe these kinetically driven processes at temperatures relevant to nuclear fireball chemistry for actinides (e.g., uranium) and other metal oxides (e.g., iron, aluminum) that may be present as structural/building materials during nuclear fireball cooling.

In our previous work, we have documented the development of a plasma flow reactor (PFR) system to study nanoparticle formation in controlled environments representing the temperature conditions of nuclear debris formation (Koroglu et al., 2017). We have characterized the temperature distribution along the PFR by computational fluid dynamics simulations and experimental measurements. Nanoparticles of various metal oxides (e.g., uranium, iron, and aluminum oxides) were synthesized using the PFR (Koroglu et al., 2018). Transmission electron microscope images of the synthesized particles were reported to show the sizes and crystal structures of the particles. The variations in particle size among various metal oxides were attributed to the interplay between kinetically driven gas phase chemical reactions and physical nanoparticle formation processes (i.e., nucleation of particles).

In the present study, to gain a better insight into the competition between kinetically driven processes (e.g., oxidation vs nucleation), we vary the cooling history (i.e., temperature vs residence time) along the PFR setup and investigate the effect of cooling time scales on the resulting sizes of the uranium, aluminum, and iron oxide particles. Two distinct rates at which the vaporized species are cooled from 5000 K to 1000 K are imposed to synthesize these materials. Scanning electron microscope images are acquired and then processed to report the size distributions of particles. Our measured size distributions are then compared to the predictions of a kinetic model that describes gas phase speciation, nucleation, condensation, and coagulation of metal oxide nanoparticles along the plasma flow reactor.

2. EXPERIMENTAL SECTION

2.1. Plasma Flow Reactor

The details of the plasma flow reactor used in this work are provided in a previous study (Koroglu et al., 2017). The schematic of the experimental setup is shown in Figure 1. The reactor consists of a 20 mm OD inductively coupled argon plasma torch attached to a 40 mm OD quartz flow reactor tube by means of an adapter (i.e., ring flow injector). The outermost, central, and innermost argon flow rates through the torch are set to 14.5, 0, and 1 l/min, respectively. Aqueous solutions of Al, Fe, or U nitrates are introduced to the plasma using a nebulizer with argon carrier gas. The ring flow injector is used to introduce argon gas downstream from the plasma to vary the cooling rate. After the argon plasma vaporizes and atomizes the aqueous analytes, the emission spectra of chemicals (e.g., Fe, AlO) were recorded using a grating spectrometer to determine the

temperature of the hot gas, as described previously (Koroglu et al., 2017). The uncertainty of the temperature measurements determined from optical emission measurements were $\pm 8\%$.

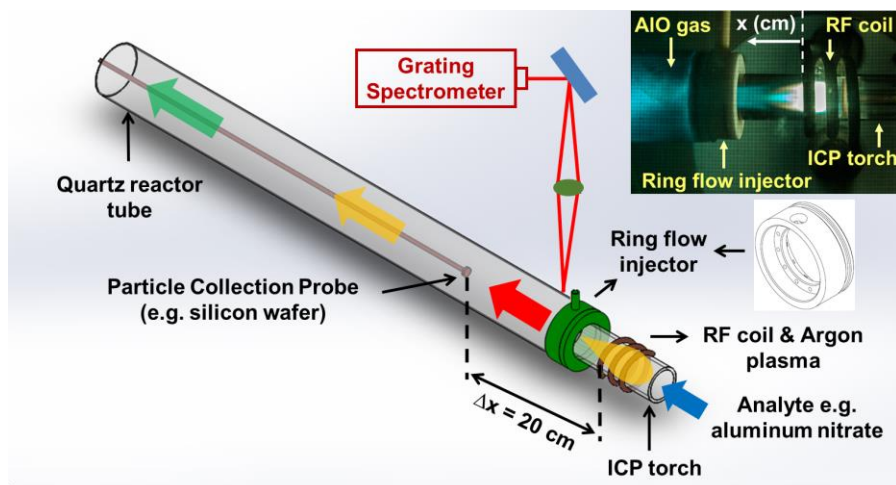


Figure 1. The schematic of the plasma flow reactor. An image of the inductively coupled argon plasma with the blue AIO gas optical emission is given in the upper right corner.

A particle collection probe inserted from the open end of the flow reactor is used to collect condensed materials on silicon wafers to analyze them *ex situ* using scanning electron microscopy. During each experiment, the collection plate was left inside the flow reactor for three minutes to allow accumulation of the metal oxide nanoparticles on the plate. The probe was positioned in the center of the flow field 20 cm from the end of the RF coil, where the gas temperature was measured using a thermocouple (± 2 K) attached to the probe. The temperature varied between 1100 and 950 K, when the ring flow rate was changed between 0 (cooling history_1) and 12.1 l/min (cooling history_2), respectively.

The concentrations of the aqueous solutions of metal nitrates are adjusted such that same number of metallic atoms are injected into the argon plasma. The iron, uranyl, and aluminum nitrate concentrations are 0.1, 0.125, and 0.087 gram of salt per milliliter of water, respectively. The resulting mass flow rates are 3.7×10^{18} atoms/min for iron and uranium, and 3.5×10^{18} atoms/min for aluminum.

In our previous work, crystal structures of the metal oxide nanoparticles synthesized using the plasma flow reactor were determined from the electron diffraction patterns measured by transmission electron microscopy (Koroglu et al., 2018). The following phases were identified: FeO-wustite, eta- Al_2O_3 , and a combination of fcc- UO_2 and alpha- UO_3 . In this study, the microscope images are processed to determine the particle size distributions of these metal oxides.

In the present study, Fe, Al, and U are studied separately under identical run conditions. An inert gas (Ar) is chosen as the carrier gas to limit the number of chemical reactions. These experimental conditions help investigate the effect of chemical species and cooling rate on particle formation processes. In future experiments, more complex systems (e.g., U + Fe) with gas mixtures that are more representative of nuclear incidents (e.g., air) can be studied.

2.2. Temperature distribution as a function of cooling rate

The velocity and temperature distributions along the plasma flow reactor are simulated using the Star CCM+ fluid dynamics code as described in our previous publication (Koroglu et al., 2017). The Reynolds numbers are low and thus the flow field is highly laminar except for the section where there is an adapter piece (i.e., ring flow injector) that allows injection of further argon gas to induce different cooling histories along the plasma flow reactor. Therefore, the turbulent k- ϵ model in the Star CCM+ fluid dynamics code was used to model this transitional fluid dynamic regime. The inductively coupled plasma was modeled by a homogeneous heat source to represent the ohmic heating of the argon gas induced by the RF field. The temperature and velocity patterns at the end of the ICP torch were used as boundary conditions at the flow reactor tube section. The subsequent heat transfer processes (e.g., radiative, convective) were also modeled using the same STAR CCM+ fluid dynamics code.

The CFD model predictions are plotted in Figure 2 for two different cooling histories: cooling history_1 and cooling history_2. In the case of cooling history_2, the gas temperature drops suddenly at 4.5 cm, which is the location of the ring flow injector. Argon gas from the ring flow injector creates a flow stream around the high-temperature core, resulting in a more streamlined flow along the reactor tube. For that reason, a smooth temperature profile is obtained for the case of cooling history_2, whereas the flow field exhibited eddies after the ring flow injector in the case of cooling history_1 due to the absence of ring flow and abrupt increase in reactor diameter from 20 to 40 mm. As a result, small fluctuations in temperature are seen in the model predictions between 5 and 20 cm locations. The modeled and measured temperatures are in good agreement.

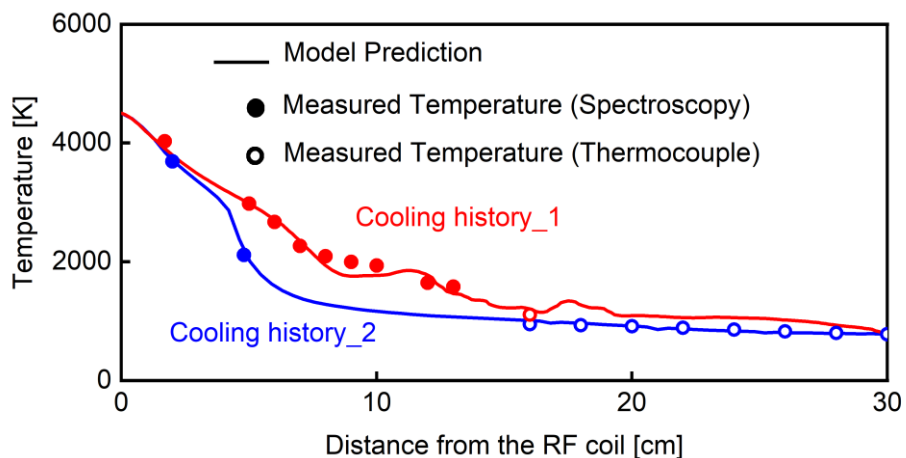


Figure 2. Comparison of measured and modeled temperature distributions as a function of distance along the plasma flow reactor for two different cooling histories: cooling history_1 and cooling history_2. The temperature data shown by the red line were published in our previous work that documented the development of the plasma flow reactor setup (Koroglu et al., 2018).

The CFD model is also used to infer the variation of temperature as a function of time. Temperature vs residence time and location are plotted for a parcel of gas injected from the center of the ICP torch and shown in Figure 3. It takes 16 ms for gas temperature to decrease from 4500 K to 2000 K in the case of cooling history_1 ($\Delta T/\Delta t \sim 156 \times 10^3$ K/s), whereas the temperature rapidly drops to the same value within 8 ms for the case of cooling history_2 ($\Delta T/\Delta t \sim 312 \times 10^3$ K/s). Note that there is a big difference in cooling rate upstream/downstream of the ring flow injector for the two different cooling histories. The rate of temperature drop in the case of cooling history_2 substantially slows down downstream of the ring flow injector, because the rapidly cooled gas moves more slowly due to its higher density and this increases the residence time of the gas inside the flow reactor. In fact, the temperature distribution in Figure 3 shows that the residence time of the gas to reach the collection plate at 20 cm is nearly three times longer for the cooling history_2 (146 ms) than for the cooling history_1 (53 ms). Therefore, the differences in cooling rates upstream/downstream of the ring flow injector and their effects on particle formation processes will be discussed in detail in the Model Predictions section.

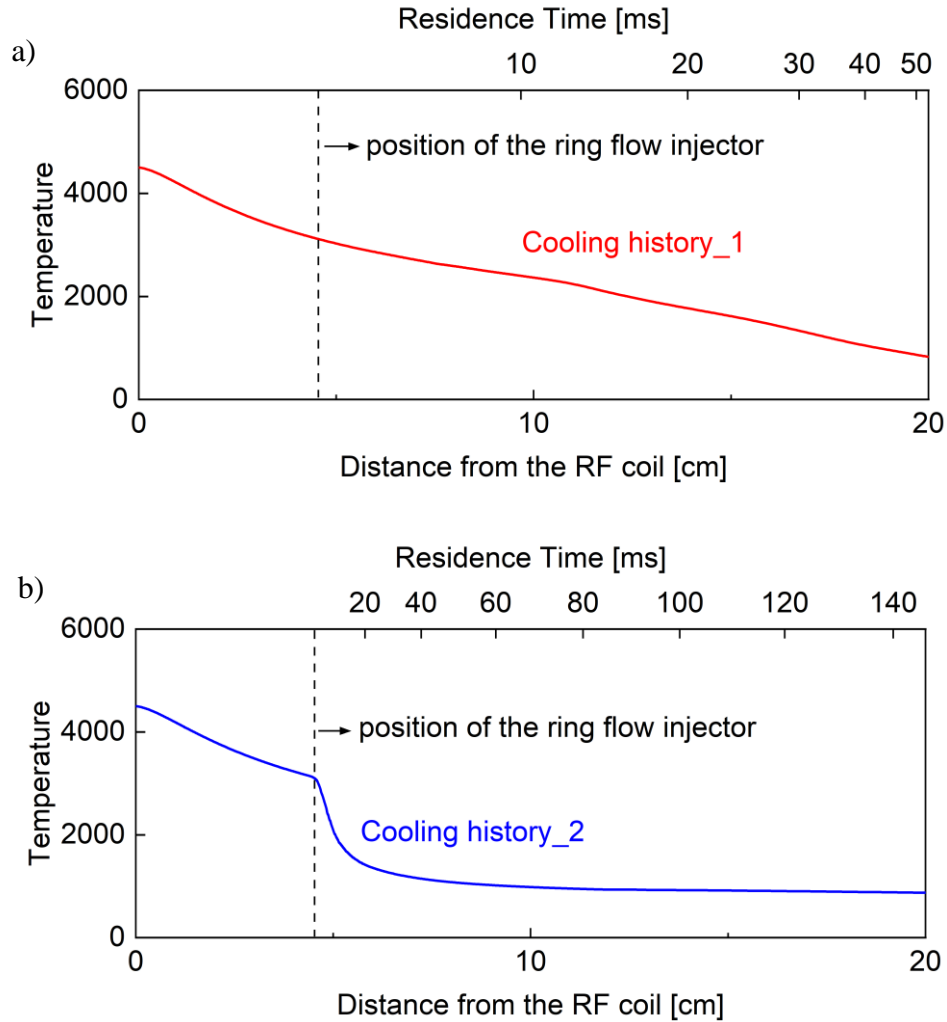


Figure 3. Comparison of modeled temperature distributions for two different cooling histories: a) cooling history_1 and b) cooling history_2. The top x-axis shows the residence time of the gas, whereas the bottom x-axis shows the distance along the plasma flow reactor. The position of the ring flow injector is around 4.5 cm.

3. DATA PROCESSING

Several SEM images taken from different regions of the silicon wafers were processed using the ImageJ software to determine the particle size distributions. Some example SEM images taken at four different magnifications ($\times 3500$, 7000 , 14000 , and 28000) are shown in Figure 4 for aluminum oxide particles collected for the cooling history_1. The SEM images were converted to binary (black/white) images and then the ImageJ software was used to detect the edges of the particles. The software allowed us to determine the sizes of the detected particles by converting the pixel size of the images to nanometers based on the scale bar given in each image. The binary

images and the detected particles from the images taken at x 3500 and x 7000 magnifications are displayed in Figures S-1 and S-2 in Supplementary Information. The images taken at low magnifications (e.g., x 3500) were used to determine the sizes of the large particles (e.g., sizes above 600 nm), whereas the higher magnification images (e.g., x 7000) were used to detect the smaller particles (e.g., sizes between 300 nm and 600nm).

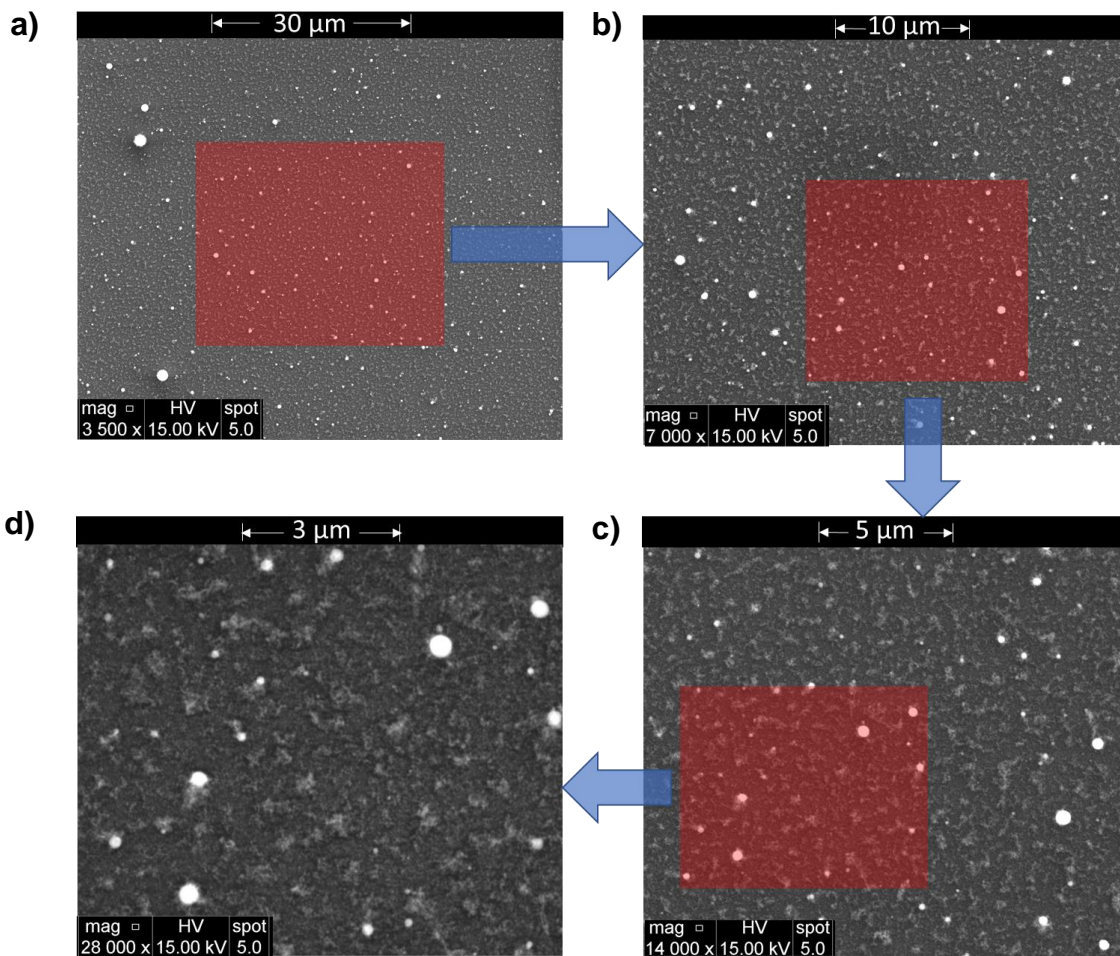


Figure 4. The SEM images of Al₂O₃ particles taken at four different magnifications: (a) x 3500, (b) x 7000, (c) x 14,000, and (d) x 28,000. The red boxes and blue arrows indicate the insets taken at different magnifications.

The image processing was performed with various magnifications of images on different areas of the silicon wafer. The size distribution of aluminum oxide particles on three separate regions of the wafer are shown as an example in Figure 5 to assess the uniformity of the size distributions across the collection plate. Some variations in distribution exist between different regions of the wafer. An overall size distribution is reported by combining the size distribution of particles from different regions of the wafer. The combined results are shown in the results section.

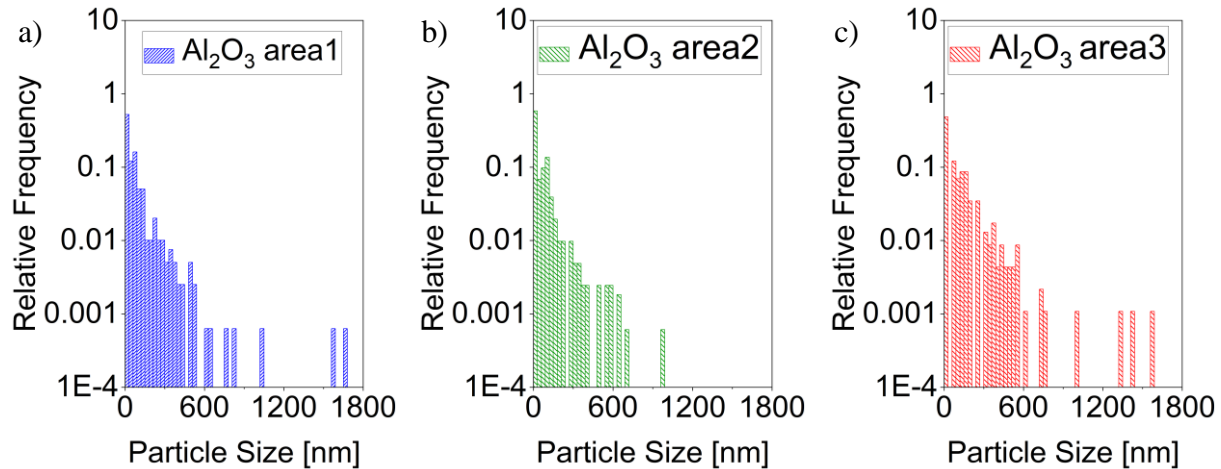


Figure 5 Comparison of measured size distributions of aluminum oxide nanoparticles obtained from three different areas on the silicon wafer for the case of cooling history_1.

4. RESULTS

4.1. Experimental Results: Nanoparticle Characteristics

4.1.1. Aluminum Oxide Particles

SEM images of aluminum oxide particles recovered at 20 cm from the end of the RF coil are shown in Figure 6 for two different cooling histories: cooling history_1 and cooling history_2. Several large and spherical particles are observed in the case of cooling history_1 (Fig. 6-a), whereas the number of large particles decreases substantially in the case of cooling history_2 (Fig. 6-b). Close-up images are displayed in Figures 6 (c) and (d) for cooling history_1 and cooling history_2, respectively. The surface of the silicon wafer shows larger features in the case of cooling history_2.

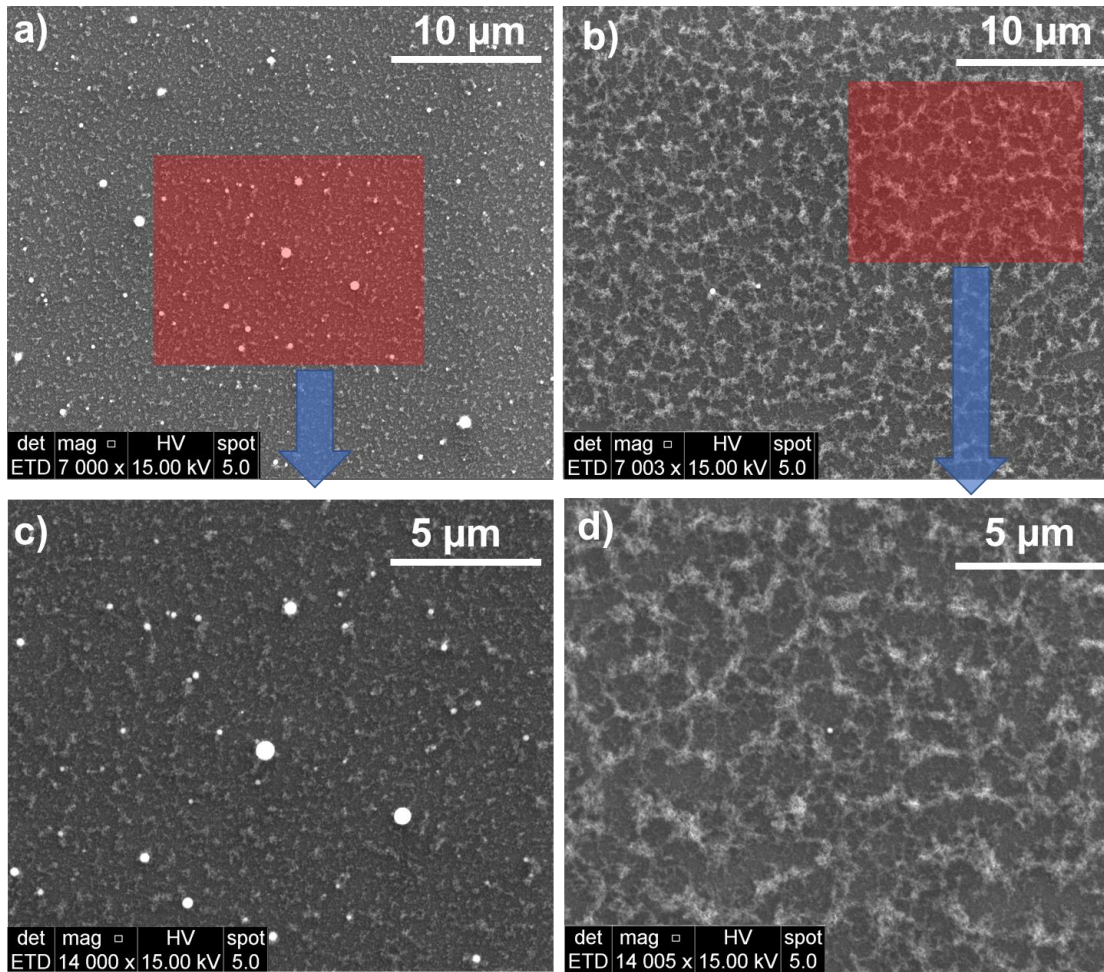


Figure 6. Comparison of SEM images of Al_2O_3 particles for two different cooling histories: a) and (c) cooling history_1 and b) and (d) cooling history_2.

4.1.2. Iron Oxide Particles

SEM images of iron oxide particles recovered at 20 cm from the end of the RF coil are given in Figure 7 for two different cooling histories: cooling history_1 and cooling history_2. Very few spherical particles of sizes around 500 nm were observed in the case of cooling history_1 (Fig. 7-a). However, these particles were not observed in the case of cooling history_2 (Fig. 7-b).

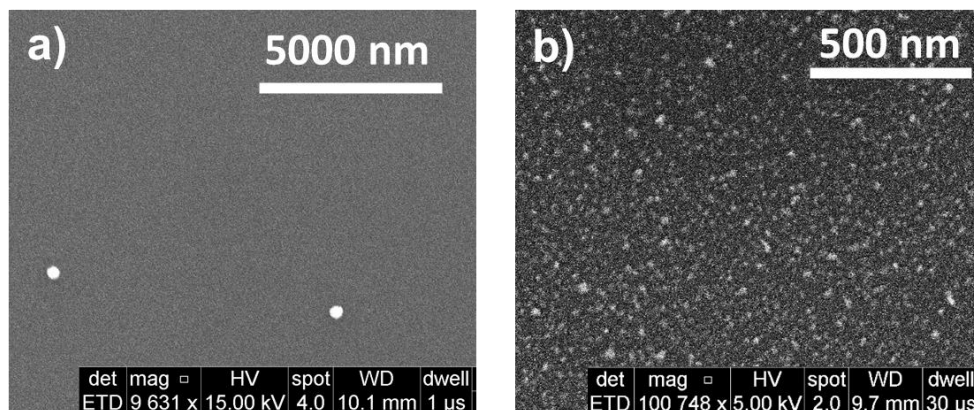


Figure 7. Comparison of SEM images of FeO particles for two different cooling histories: a) cooling history_1 and b) cooling history_2.

4.1.3. Uranium Oxide Particles

The SEM images of uranium oxide particles recovered at 20 cm from the end of the RF coil are given in Figures 8 (a) and (b) for the cases of cooling history_1 and cooling history_2, respectively. The variation in cooling histories do not seem to affect the sizes of the uranium oxide particles. Small and irregularly shaped uranium oxide particles are seen in both cases (10-30 nm).

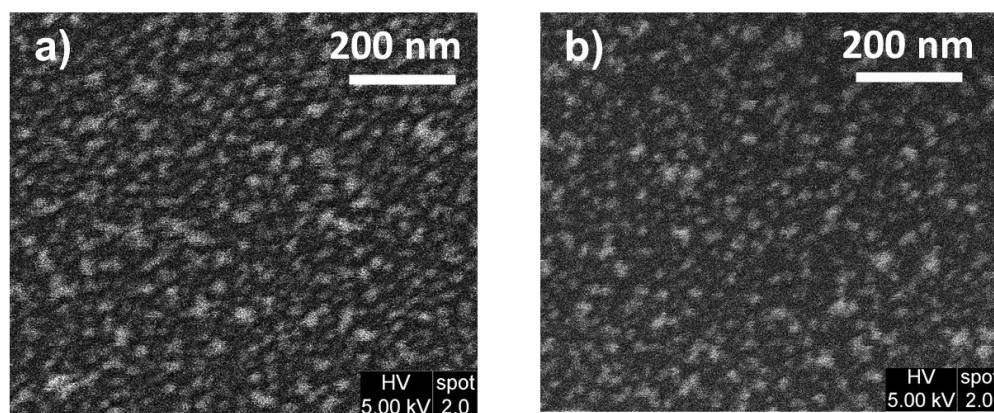


Figure 8. Comparison of SEM images of UO₂/UO₃ particles for two different cooling histories: a) cooling history_1 and b) cooling history_2.

4.2. Measured Size Distribution of Particles

The aluminum and iron oxide particles have well-defined shapes in the case of cooling history_1 as shown in Figures 6 (a) and 7 (a), whereas those of uranium oxide are very irregular (see Figure 8). Therefore, a circular size cannot be assigned to an individual uranium oxide particle. Nevertheless, the SEM images clearly show that even the irregular aggregates of the uranium oxide particles are always less than 30 nm. Therefore, a bin size of 30 nm is chosen to report the size

distributions of particles so that a quantitative comparison can be made among three different metal oxides. The resulting size distributions of the particles for the case of cooling history_1 are shown in Figure 9. The aluminum oxide particles exhibited the broadest size distribution among the three metal oxides studied. The mean particle diameters and standard deviations are determined to be 38 nm (SD = 54 nm) and 73 nm (SD = 111 nm) for iron and aluminum oxides, respectively.

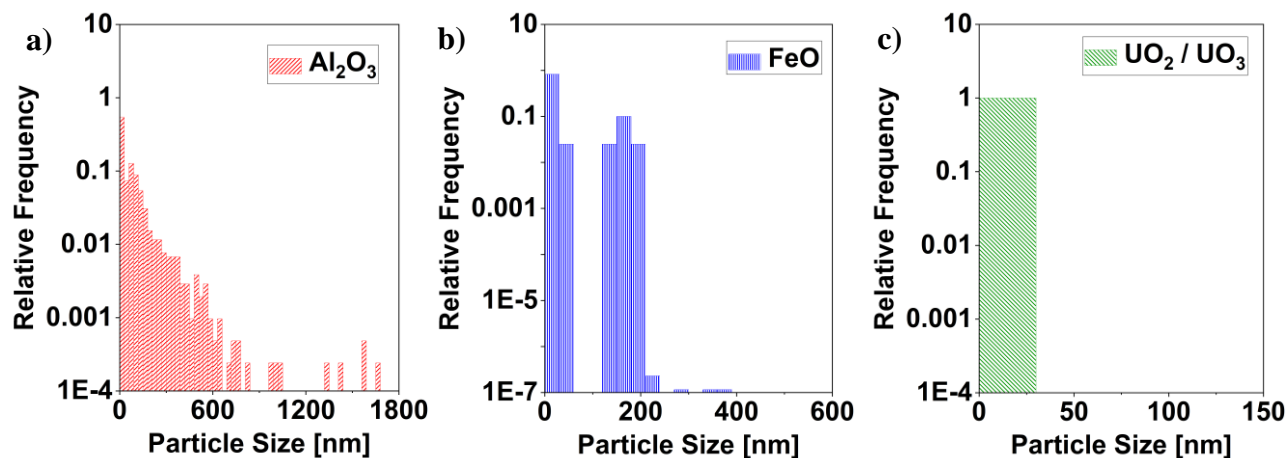


Figure 9. Measured size distributions of a) aluminum, b) iron, and c) uranium oxide nanoparticles for the case of cooling history_1.

A similar quantitative size distribution analysis has been difficult to perform using the microscope images taken at cooling history_2, because even the aluminum oxide particles become very irregular under those conditions as seen in Figures 6 (b) and (d). In the present study, more rapid cooling decreased the largest sizes of the aluminum and iron oxide particles observed (Figures 6 and 7), whereas there is not any noticeable change in the sizes of the uranium oxide particles (Figure 8). Uranium oxidation and subsequent processes of particle formation from vapor phase begin in the high-temperature region close to the RF coil (G. V. Samsonov, 1982; Koroglu et al., 2018), and therefore these processes might be largely unaffected by variations in temperature gradients induced after the ring flow injector at $x = 4.5$ cm. However, the aluminum and iron oxide particles form at lower temperatures (Koroglu et al., 2018) downstream of the flow reactor tube, and thus the differences in thermal gradients between different cooling histories might have a greater influence on the particle growth kinetics for these metals.

In the literature, the effect of increased cooling rate was reported to result in more uniformly distributed smaller particles for different kinds of metals and oxides (e.g., Cr, TiO_2) (Ealias & Saravanakumar, 2017; Leparoux et al., 2005; Li & Ishigaki, 2001; Meyyappan, 2011; Shin et al.,

2006; Yamamuro et al., 1999). However, a detailed model was not built in these past studies to investigate which kinetically driven processes are responsible for these changes. In the current work, we developed a kinetic model to study the effects of two different cooling rates on the size distributions of iron, aluminum, and uranium oxides. The model and its predictions are discussed in the next section.

4.3. Model Predictions

The kinetic model developed herein couples gas-phase oxidation chemistry with particle formation for iron, aluminum and uranium oxides. The O-H chemistry is taken from the work of Li et al. (Li et al., 2017), while the chemistry involving N-H-O is from the work of Glarborg et al. (Glarborg et al., 2018). The relationship between gas phase chemical speciation and homogeneous nucleation from vapor phase was analyzed using a chemical kinetic model in our previous work for iron and aluminum oxides (Koroglu et al., 2018). In the present study, we further develop the model by refining the kinetic rate calculations for these processes. We extend our calculations to model the uranium gas-phase oxidation and particle formation from vapor phase. The rates of the uranium oxidation reactions are taken from our previous theoretical work on uranium plasma chemistry (Finko et al., 2017a). The rate coefficients and the associated references for all three metals are given in Table 1.

In this model, particle nucleation, condensation and coagulation processes are treated as kinetic reactions by discretizing the particle size distribution using a sectional method and treating the resulting “BINs” as equivalent species (Pope & Howard, 1997). The processes of nucleation, condensation, and coagulation are represented as sets of molecule-molecule, molecule-BIN, and BIN-BIN reactions, respectively. Therefore, this approach does not utilize classical nucleation theory, instead treating nucleation as a series of binary hard-sphere collisions expressed in reaction form as:



where A and B denote molecules or molecular clusters smaller than the first sectional BIN BIN_1 and $c_1 = (m_A + m_B)/m_{BIN_1} - 1$ and $c_2 = 1 - c_1$ are stoichiometric coefficients that enforce mass conservation.

Table 1: Reaction mechanisms for gas phase metal oxide formation based on first order rate estimates and literature for iron (Smirnov, 2012), aluminum (Catoire et al., 2003; Y. Huang et al., 2009; Starik et al., 2015), and uranium (Finko et al., 2017b).

No.	Reaction	k (cm ³ /s) ^a
Iron oxidation		
1	$\text{Fe} + \text{O}_2 \rightleftharpoons \text{FeO}_2$	$1.9927 \times 10^{-10} \exp(-2646/T)$
2	$\text{Fe} + \text{O} \rightleftharpoons \text{FeO}$	1.6606×10^{10}
3	$\text{Fe} + \text{FeO}_2 \rightleftharpoons \text{FeO} + \text{FeO}$	1.6606×10^{10}
4	$\text{FeO} + \text{O} \rightleftharpoons \text{Fe} + \text{O}_2$	2.9060×10^{11}
5	$\text{FeO} + \text{O} \rightleftharpoons \text{FeO}_2$	1.6606×10^{10}
6	$\text{FeO}_2 + \text{O} \rightleftharpoons \text{FeO} + \text{O}_2$	1.6606×10^{10}
Aluminum oxidation		
7	$\text{Al} + \text{O}_2 \rightleftharpoons \text{AlO} + \text{O}$	$1.61 \times 10^{-10} \exp(-80.5/T)$
8	$\text{Al} + \text{O} + \text{M} \rightleftharpoons \text{AlO} + \text{M}$	$8.27 \times 10^{-31}/T$
9	$\text{AlO} + \text{O}_2 \rightleftharpoons \text{AlO}_2 + \text{O}$	$7.672 \times 10^{-10} \exp(-10008/T)$
10	$\text{Al}_2\text{O}_3 \rightleftharpoons \text{Al}_2\text{O}_2 + \text{O}$	$3.00 \times 10^{15} \exp(-49144.4/T)$
11	$\text{Al}_2\text{O}_3 \rightleftharpoons \text{AlO}_2 + \text{AlO}$	$3.00 \times 10^{15} \exp(-63915.4/T)$
12	$\text{Al}_2\text{O}_2 \rightleftharpoons \text{AlO} + \text{AlO}$	$1.00 \times 10^{15} \exp(-59335.7/T)$
13	$\text{Al}_2\text{O}_2 \rightleftharpoons \text{Al} + \text{AlO}_2$	$1.00 \times 10^{15} \exp(-74937.1/T)$
14	$\text{Al}_2\text{O}_2 \rightleftharpoons \text{Al}_2\text{O} + \text{O}$	$1.00 \times 10^{15} \exp(-52466.0/T)$
15	$\text{AlO}_2 \rightleftharpoons \text{AlO} + \text{O}$	$1.00 \times 10^{15} \exp(-44564.6/T)$
16	$\text{Al}_2\text{O} \rightleftharpoons \text{AlO} + \text{Al}$	$1.00 \times 10^{15} \exp(-67035.7/T)$
Uranium oxidation		
17	$\text{U} + \text{O}_2 \rightleftharpoons \text{UO} + \text{O}$	$3.36 \times 10^{-12} T^{1/2} \exp(-5161.70/T)$
18	$\text{U} + \text{O}_2 \rightleftharpoons \text{UO}_2$	$3.36 \times 10^{-12} T^{1/2} \exp(-12910.0/T)$
19	$\text{UO} + \text{O}_2 \rightleftharpoons \text{UO}_2 + \text{O}$	$3.8 \times 10^{-11} T^{1/6}$
20	$\text{UO}_2 + \text{O}_2 \rightleftharpoons \text{UO}_3 + \text{O}$	$1.17 \times 10^{-11} T^{1/2} \exp(-89157.0/T)$
21	$\text{U}_2\text{O}_3 \rightleftharpoons \text{U}_2\text{O}_2 + \text{O}$	$3.00 \times 10^{15} \exp(-68148.6/T)$
22	$\text{U}_2\text{O}_3 \rightleftharpoons \text{UO}_2 + \text{UO}$	$3.00 \times 10^{15} \exp(-46023.3/T)$
23	$\text{U}_2\text{O}_3 \rightleftharpoons \text{UO}_3 + \text{U}$	$3.00 \times 10^{15} \exp(-64746.0/T)$
24	$\text{U}_2\text{O}_2 \rightleftharpoons \text{UO} + \text{UO}$	$1.00 \times 10^{15} \exp(-60010.1/T)$
25	$\text{U}_2\text{O}_2 \rightleftharpoons \text{U} + \text{UO}_2$	$1.00 \times 10^{15} \exp(-61175.1/T)$
26	$\text{UO}_3 \rightleftharpoons \text{UO} + \text{O}_2$	$1.00 \times 10^{15} \exp(-90465.3/T)$
27	$\text{UO}_3 \rightleftharpoons \text{UO}_2 + \text{O}$	$1.00 \times 10^{15} \exp(-73300.3/T)$
28	$\text{UO}_2 \rightleftharpoons \text{UO} + \text{O}$	$1.00 \times 10^{15} \exp(-93229.8/T)$

^a 1/s and cm⁶/s for unimolecular and three-body reactions, respectively.

The corresponding kinetic rate coefficient is equivalent to a free molecular collision frequency:

$$k_{FM} = \pi(r_A + r_B)^2 \sqrt{\bar{c}_A^2 + \bar{c}_B^2}$$

where r and $\bar{c} = \sqrt{8k_B T / \pi m}$ are the collision radii and thermal velocities of the colliding particles, respectively. The corresponding reaction rate would then be $R_{FM} = k_{FM} n_A n_B$ where n denotes the number density of a given species. The radii of the colliding particles are calculated via a power law interpolation (Sharipov A. S. et al., 2013) (i.e. $r_i = r_0 i^x$ for an i -mer) between the combined Van der Waals volumes (Savel'ev & Starik, 2017) of the constituent atoms (i.e. $r = (\sum_a r_a^3)^{1/3}$) for the nuclei particles and the bulk liquid density (i.e. $r = (3m_i / 4\pi\rho)^{1/3}$) for the liquid-like clusters ($r > 5$ nm). The particle size corresponding to the first BIN is a fixed parameter in the model and is chosen as the number of oxide molecules (i.e., Al_2O_3 , FeO , or UO_3) in the smallest stable molecular cluster. This number lies in the range of 4-8 monomers and is based partly on the local minima of bond dissociation energies for Fe (Armentrout, 2001), FeO (Gutsev et al., 2017), and UO_3 (Marks et al., 2020) as well as on density-functional-theory (DFT) studies of the transition to liquid-like clusters for Al_2O_3 (Savel'ev & Starik, 2018). We found that changing the nucleating BIN size between 4 and 16 monomers had little impact on the resulting size distributions. Therefore, the first BIN size was fixed at 4 monomers here to reduce computational times. A geometric constraint on the BIN sizes is enforced by setting the mass of each subsequent BIN to double that of the previous one (i.e., $m_i = m_0 2^i$). In total, 36 BINs were included in the size distribution, with particles diameters spanning from less than a nanometer to a few microns.

Similar to nucleation, condensation is also treated as a kinetic process equivalent to:



that is, it is a process wherein particles of size BIN_i grow via condensation of molecules A (with $c_2 = m_A / m_{\text{BIN}_i}$ and $c_1 = 1 - c_2$ again conserving mass). Although it is often assumed that condensing particles are much smaller than the target particles (i.e., $r_A \ll r_i$), this assumption cannot be made here due to the small nucleation sizes considered. Therefore, the rate coefficient for condensation is expressed in a transition formulation:

$$k_{cond} = \left(\frac{1}{k_{CC}} + \frac{1}{k_{FM}} \right)^{-1}$$

where k_{FM} is the free molecular collision rate as explained above and k_{CC} is the continuum condensation rate coefficient given by:

$$k_{CC} = 4\pi(r_A + r_i)(D_{A,CE} + D_{i,SF})$$

where $D_{A,CE}$ is the Chapman-Enskog binary diffusion coefficient (D. D. Huang & Seinfeld, 1988) for the molecule:

$$D_A = \frac{3\pi}{32}(1+z)\lambda_{Ag}\bar{c}_A$$

where $z = m_A/m_g$ is the mass ratio of the vapor molecule to the bath gas (argon here), \bar{c} is again the thermal velocity, and the λ_{Ag} is the mean free path of the vapor in the bath gas given by:

$$\lambda_{Ag} = \left(\sqrt{1+zn_g}\pi(r_A+r_g)^2\right)^{-1}$$

where n is again a number density and r are collision radii. The particle diffusion coefficient $D_{i,SF}$ is instead given by the slip corrected Stokes-Einstein coefficient:

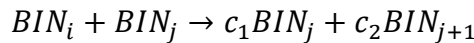
$$D_{i,SF} = C_i \frac{k_B T}{6\pi r_i \eta_g}$$

where η_g is the bath gas viscosity and C_i is the slip flow correction factor estimated here using the Phillips form:

$$C_i = \frac{5 + 4Kn_i + 6Kn_i^2 + 18Kn_i^3}{5 - Kn_i + (8 + \pi)Kn_i^2}$$

where $Kn_i = \lambda_g/r_i$ is the Knudsen number expressed in terms of the bath gas mean free path $\lambda_g = 1/4\sqrt{2}\pi n_g r_g^2$. Note that the reduction in the condensation rate due to evaporation is not included here as it was found to have little impact on the size distribution for the conditions considered here.

Finally, the coagulation rate coefficient is given by the reaction:



where $j \geq i$, $c_2 = m_{BIN_i}/m_{BIN_j}$, and $c_1 = 1 - c_2$. Again, the rate coefficient is given by a harmonic mean expression:

$$k_{coag} = \left(\frac{1}{k_{SF}} + \frac{1}{\gamma_{coll}\gamma_{coag}k_{FM}} \right)^{-1}$$

where k_{SF} is the slip-flow corrected continuum rate coefficient given by:

$$k_{SF} = 4\pi(r_i + r_j)(D_{i,SF} + D_{j,SF})$$

and γ_{coll} and γ_{coag} are the collision enhancement and coagulation efficiency factors due to short- and long-range interatomic forces. Here, we have used a collision enhancement factor due to Sceats (Sceats, 1989) and a coagulation efficiency factor due to Hou (Hou et al., 2020). Although more advanced approximations of the enhancement factor are available (Ouyang et al., 2012), we found that the Sceats estimate fell within 15% of these approximations (resulting in minimal differences in the modeled size distributions) but could be more conveniently expressed as a modification to the kinetic coagulation rates.

The 0-D homogeneous closed reactor module of ANSYS Chemkin-Pro with constrained pressure and temperature was used to model the experiments. Constant atmospheric pressure was assumed in all calculations. Temperature as a function of residence time (see Fig. 3) was specified using the history of a representative parcel of gas from the computational fluid dynamic simulations. The concentrations of chemical species in three different experiments (Experiments I, II, III) are summarized in Table 2 and were used as the initial conditions in the kinetic model. It is assumed that the metal nitrate hydrates dissociate completely to elemental components, because the mixture is passing through the plasma torch and experiencing temperatures as high as 5000 K.

Table 2. Mole fractions of chemical species at the inlet of the plasma flow reactor

Experiment No	O	H	N	Ar	Fe	Al	U
I	0.03329	0.06417	0.00041	0.90199	0.000136	-	-
II	0.03312	0.06394	0.00038	0.90240	-	0.000128	-
III	0.03278	0.06336	0.00027	0.90350	-	-	0.000137

The analyte is diluted through the innermost argon flow (i.e., 1 L/min) from the nebulizer gas line. For the case of cooling history_1, this concentration remains constant throughout the reactor

until the sampling plate located at 20 cm from the end of the RF coil. In the case of cooling history_2, there is argon flow (12.1 L/min) through the ring flow injector, which induce mixing and dilution of the reactants with the outermost flow (i.e. 14.5 L/min). Therefore, the ‘reactor network’ approach is used to simulate the kinetics of particle formation processes at two different cooling histories, as shown by the schematic in Figure 10.

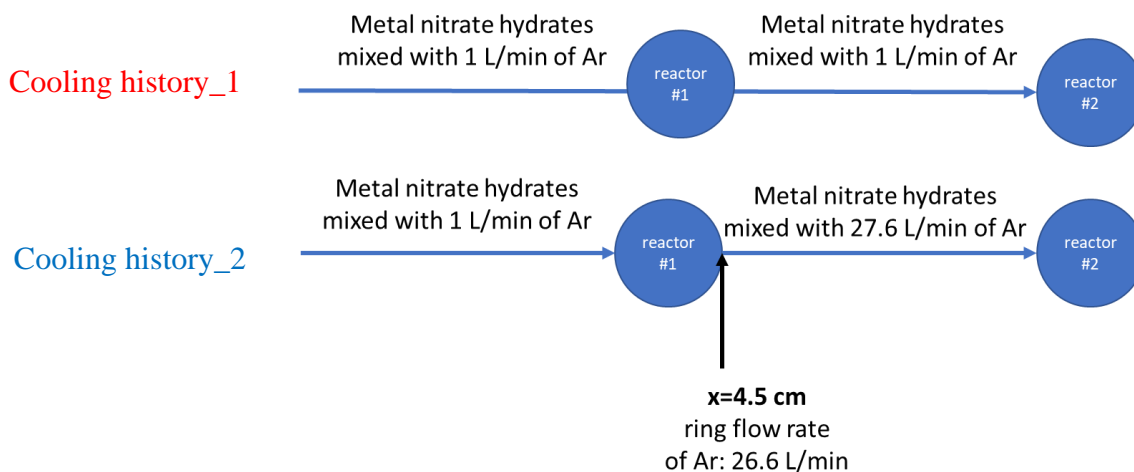


Figure 10. Schematic of the ‘reactor network’ approach used in the kinetic simulations of two different cooling histories: cooling history_1 and cooling history_2

In the case of cooling history_2, a first reactor is used to simulate the chemical reactions in the section of the flow reactor ahead of the ring flow injector. The resulting mixture is then taken, mixed with an Ar flow corresponding to the outermost flow and ring flow rates, and then fed into a second reactor to simulate the rest of the process. The predicted concentrations of chemical species as a function of time obtained from the CHEMKIN simulations were then transformed back to an axial distance via a coordinate transformation informed by the CFD simulation.

Figure 11 shows the results of the kinetic simulations in terms of particle size distributions (PSD) for the three metal oxides collected at 20 cm position. The kinetic simulations accurately predict the trends observed in our experimental measurements. Smaller particles are produced in the case of cooling history_2, because the additional argon gas through the ring flow injector dilutes the gas mixture and slows down the reactivity of chemicals. Although the residence time of the reactants at the particle collection plate ($x = 20$ cm) is three times longer in the case of cooling history_2, the effect of dilution is strong enough to prevent further particle growth. This results in mean particle sizes of around 11, 13, and 7 nm for iron, aluminum, and uranium oxide

particles, respectively. In the case of cooling history_1, the mean particle sizes as large as 20, 26, and 19 nm are predicted for iron, aluminum, and uranium oxide particles, respectively.

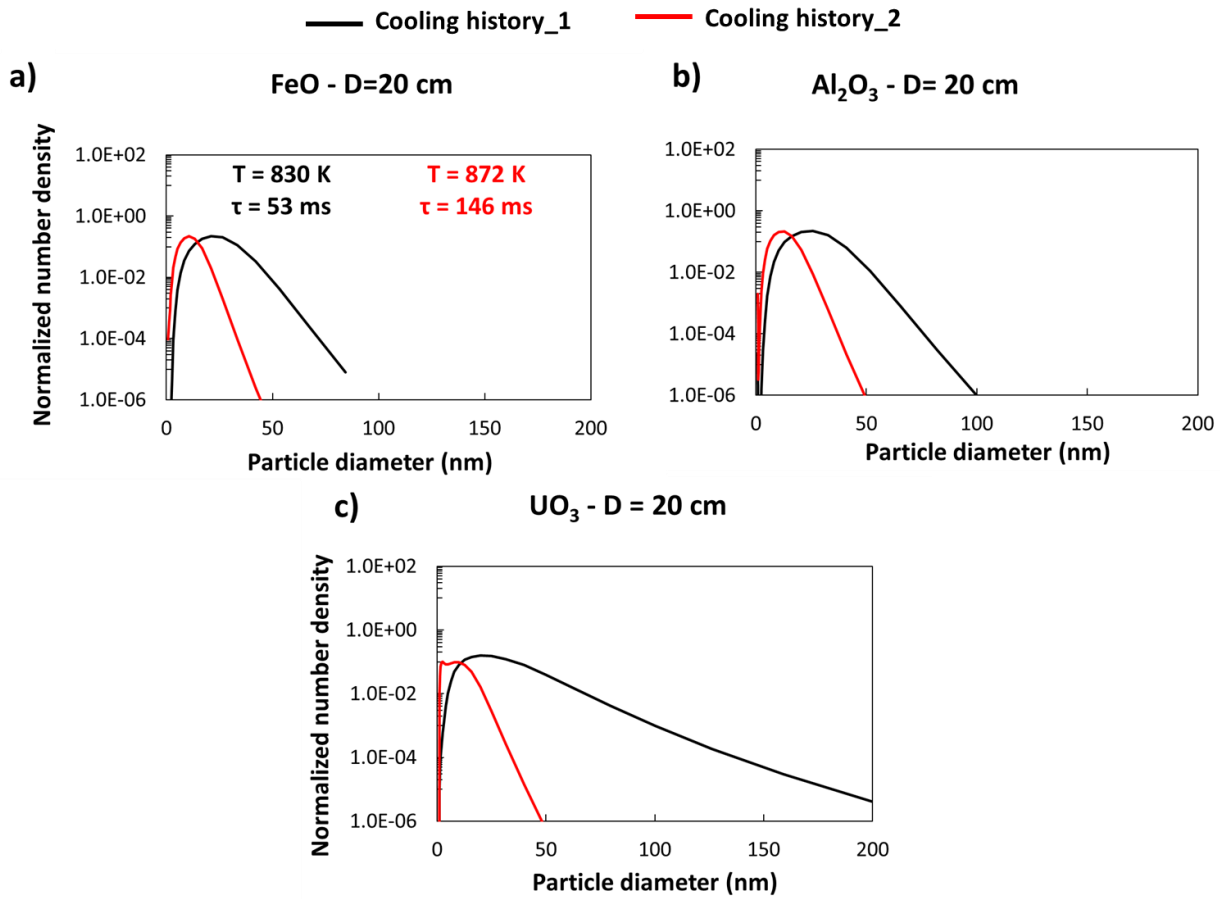


Figure 11. Predictions of normalized particle size distributions for (a) iron oxide, (b) aluminum oxide, and (c) uranium oxide particles at 20 cm away from the RF coil. The black lines are used for the simulation results obtained with the temperature distribution given by the cooling history_1, whereas the red lines correspond to those given by the cooling history_2.

The kinetic simulations also show that the mean aluminum oxide particle size is bigger than that of the iron oxide particles, which is in line with the experimental observations. However, the predicted PSD for uranium oxide particles is quite bigger than what is observed in our experimental measurements. This could be due to various reasons. Our recent measurement results with a similar experimental setup show the presence of both UO_2 and UO_3 particles (Koroglu et al., 2020). However, the current kinetic model predicts that all the uranium metals will eventually be converted to UO_3 particles by the time they hit the collection plate. This indicates further experimental data is needed to better constrain the rates of the kinetically limited processes, including gas phase uranium oxidation and nucleation of particles.

There are various other reasons that could help achieve a better quantitative agreement between the current simulation results and experimental measurements. According to the CFD model it takes about 0.050 s for the gas to travel from the RF coil to the particle collection plate ($x = 20$ cm) in the case of cooling history_1. However, the collection plate was kept inside the flow reactor for 180 seconds during the experiments before any *ex situ* analysis was performed. Therefore, the continuous accumulation of the nanoparticles is completely neglected in the current kinetic model. This suggests that future CFD simulations should account for the presence of the collection plate and the associated particle aggregation/deposition effects. Furthermore, if the size distribution data is acquired at different locations (i.e., temperatures) along the flow reactor tube, it would better constrain the kinetically driven particle formation processes (e.g., condensation vs coagulation). It would also be more accurate to compare the predictions to size distributions that are measured *in situ* rather than *ex situ*, because the two results can differ due to surface deposition effects (e.g., inertial impaction, Brownian diffusion). When the particles are large, they can deviate from the fluid streamlines that are bending around the collection plate and collide with the plate via inertial impaction (Noll & Pilat, 1970). A study of soot nanoparticle deposition found that large particles were more likely to “stick” to surfaces, shifting the size distribution towards larger particle sizes (D’Alessio et al., 2005). When the particles are small, they will follow the fluid streamlines. In that case, the particles may deposit on the plate via Brownian diffusion (Flagan & Seinfeld, n.d.; Jafari et al., 2010). Therefore, a collection efficiency can be calculated as a function of particle size in a future study to predict the fraction of “*in-situ*” particles that impact the plate. Also, there are other areas where improvements in the CFD model can help better match the experimental results. Our CFD model uses a single Lagrangian temperature profile to predict the size distributions. The rate of particle growth is very sensitive to local temperature conditions; therefore, a 3-D temperature distribution wherein all the radial and axial gradients are accounted for would result in more accurate model predictions. Lastly, our model does not consider the particle deposition on the reactor tube (i.e., wall loss) and its effect on vapor concentration and subsequent particle growth.

5. CONCLUSIONS

In this study we synthesized uranium, aluminum, and iron oxide nanoparticles from gas phase metals under varying conditions of cooling rates and obtained experimental particle size data to

advance our understanding of the particle growth processes that occur at temperatures relevant to nuclear incidents. The vaporized uranium, aluminum, and iron metals are cooled from 5000 K to 1000 K at two distinct cooling histories along a plasma flow reactor setup. The condensed particles are collected at a fixed location (i.e., fixed temperature) and analyzed using scanning electron microscopy. The microscope images are processed to obtain size distribution data. The experimental results show that the aluminum oxide particles exhibit a very broad size range compared to iron and uranium oxides. Also, the sizes of the largest aluminum and iron oxide particles observed decrease as the cooling rate during synthesis is increased, whereas significant size variations with cooling rate is not observed for uranium oxide particles.

The particle size distribution data obtained from controlled experiments is important for developing a kinetic model that describes particle growth processes during nuclear fireball condensation. In this study, a kinetic model is developed to describe the gas phase oxidation of metals and subsequent processes of nucleation, condensation, and coagulation of nanoparticles. The simulations accurately predict the experimentally observed trends of particle size variation with cooling rate. Various areas are also highlighted for further research to improve the quantitative agreement between the measurements and predictions.

ACKNOWLEDGMENTS

We are very thankful to Jenny Matzel, Joe Morris, and Al Nichols for their insightful discussions on the physical processes of nucleation, condensation, and agglomeration of particles. Funding was provided by Laboratory Directed Research and Development (LDRD) grant 20-SI-006 (K. Knight, PI). D. Curreli and H. Radousky used funding from DTRA Basic Science Grant HDTRA1-16-1-0020 (D. Curreli, PI) to help data interpretation. This work was performed under the auspices of the U.S. Department of Energy by Lawrence Livermore National Laboratory under Contract DE-AC52-07NA27344.

REFERENCES

- Armentrout, P. (2001). Reactions and Thermochemistry of Small Transition Metal Cluster Ions. *Annual Review of Physical Chemistry*, 52(1), 423–461.
<https://doi.org/10.1146/annurev.physchem.52.1.423>
- Catoire, L., Legendre, J.-F., & Giraud, M. (2003). Kinetic Model for Aluminum-Sensitized Ram Accelerator Combustion. *Journal of Propulsion and Power*, 19(2), 196–202.
<https://doi.org/10.2514/2.6118>

- D'Alessio, A., Barone, A. C., Cau, R., D'Anna, A., & Minutolo, P. (2005). Surface deposition and coagulation efficiency of combustion generated nanoparticles in the size range from 1 to 10nm. *Proceedings of the Combustion Institute*, 30(2), 2595–2603. <https://doi.org/10.1016/j.proci.2004.08.267>
- Ealias, A. M., & Saravanakumar, M. P. (2017). *A review on the classification, characterisation, synthesis of nanoparticles and their application*. 263.
- Finko, M. S., Curreli, D., Weisz, D. G., Crowhurst, J. C., Rose, T. P., Koroglu, B., Radousky, H. B., & Armstrong, M. R. (2017a). *A model of early formation of uranium molecular oxides in laser-ablated plasmas*. 50(48).
- Finko, M. S., Curreli, D., Weisz, D. G., Crowhurst, J. C., Rose, T. P., Koroglu, B., Radousky, H. B., & Armstrong, M. R. (2017b). *A model of early formation of uranium molecular oxides in laser-ablated plasmas* (No. 48). 50(48), Article 48.
- Flagan, R. C., & Seinfeld, J. H. (n.d.). *Fundamentals of air pollution engineering*.
- Freiling, E. C. (1961). Radionuclide Fractionation in Air-Burst Debris. *Science*, 133.
- G. V. Samsonov. (1982). *The Oxide Handbook* (Second Edition).
- Gelbard, F., & Seinfeld, J. H. (1979). The general dynamic equation for aerosols. Theory and application to aerosol formation and growth. *Journal of Colloid and Interface Science*, 68(2), 363–382. [https://doi.org/10.1016/0021-9797\(79\)90289-3](https://doi.org/10.1016/0021-9797(79)90289-3)
- Glarborg, P., Miller, J. A., Ruscic, B., & Klippenstein, S. J. (2018). Modeling nitrogen chemistry in combustion. *Progress in Energy and Combustion Science*, 67, 31–68. <https://doi.org/10.1016/j.pecs.2018.01.002>
- Gutsev, G. L., Belay, K. G., Gutsev, L. G., & Ramachandran, B. R. (2017). Geometrical and magnetic structure of iron oxide clusters (FeO)_n for n>10. *Computational Materials Science*, 137(Supplement C), 134–143. <https://doi.org/10.1016/j.commatsci.2017.05.028>
- Hou, D., Zong, D., Lindberg, C. S., Kraft, M., & You, X. (2020). On the coagulation efficiency of carbonaceous nanoparticles. *Journal of Aerosol Science*, 140, 105478. <https://doi.org/10.1016/j.jaerosci.2019.105478>
- Huang, D. D., & Seinfeld, J. H. (1988). On the relation between binary diffusivity and mean free path. *Journal of Colloid and Interface Science*, 125(2), 733–735. [https://doi.org/10.1016/0021-9797\(88\)90042-2](https://doi.org/10.1016/0021-9797(88)90042-2)
- Huang, Y., Risha, G. A., Yang, V., & Yetter, R. A. (2009). Effect of particle size on combustion of aluminum particle dust in air. *Combustion and Flame*, 156(1), 5–13. <https://doi.org/10.1016/j.combustflame.2008.07.018>
- Jafari, S., Salmanzadeh, M., Rahnama, M., & Ahmadi, G. (2010). Investigation of particle dispersion and deposition in a channel with a square cylinder obstruction using the lattice Boltzmann method. *Journal of Aerosol Science*, 41(2), 198–206. <https://doi.org/10.1016/j.jaerosci.2009.10.005>
- Koroglu, B., Dai, Z., Finko, M., Armstrong, M. R., Crowhurst, J. C., Curreli, D., Weisz, D. G., Radousky, H. B., Knight, K. B., & Rose, T. P. (2020). Experimental Investigation of Uranium Volatility During Vapor Condensation. *Analytical Chemistry*. <https://doi.org/10.1021/acs.analchem.9b05562>
- Koroglu, B., Mehl, M., Armstrong, M. R., Crowhurst, J. C., Weisz, D. G., Zaug, J. M., Dai, Z., Radousky, H. B., Chernov, A., Ramon, E., Stavrou, E., Knight, K., Fabris, A. L., Cappelli, M. A., & Rose, T. P. (2017). Plasma flow reactor for steady state monitoring of physical and chemical processes at high temperatures. *Review of Scientific Instruments*, 88(9), 093506. <https://doi.org/10.1063/1.5001346>

- Koroglu, B., Wagnon, S., Dai, Z., Crowhurst, J. C., Armstrong, M. R., Weisz, D., Mehl, M., Zaug, J. M., Radousky, H. B., & Rose, T. P. (2018). Gas Phase Chemical Evolution of Uranium, Aluminum, and Iron Oxides. *Nature-Scientific Reports*, 8(1), 10451. <https://doi.org/10.1038/s41598-018-28674-6>
- Leparoux, M., Schreuders, C., Shin, J.-W., & Siegmans, S. (2005). Induction Plasma Synthesis of Carbide Nano-Powders. *Advanced Engineering Materials*, 7(5), 349–353.
- Li, & Ishigaki, T. (2001). Synthesis of Crystalline Micron Spheres of Titanium Dioxide by Thermal Plasma Oxidation of Titanium Carbide. *Chemistry of Materials*, 13(5), 1577–1584. <https://doi.org/10.1021/cm000893u>
- Li, Y., Zhou, C.-W., & Curran, H. J. (2017). An extensive experimental and modeling study of 1-butene oxidation. *Combustion and Flame*, 181, 198–213. <https://doi.org/10.1016/j.combustflame.2017.03.023>
- Loyalka, S. K. (1983). Mechanics of aerosols in nuclear reactor safety: A review. *Progress in Nuclear Energy*, 12(1), 1–56. [https://doi.org/10.1016/0149-1970\(83\)90024-0](https://doi.org/10.1016/0149-1970(83)90024-0)
- Marks, J. H., Kahn, P., Vasiliu, M., Dixon, D. A., & Duncan, M. A. (2020). Photodissociation and Theory to Investigate Uranium Oxide Cluster Cations. *The Journal of Physical Chemistry A*, 124(10), 1940–1953. <https://doi.org/10.1021/acs.jpca.0c00453>
- Meyyappan, M. (2011). *Plasma nanotechnology: Past, present and future*. 44(17).
- Moody, K. J., Grant, P. M., & Hutcheon, I. D. (2015). *Nuclear Forensic Analysis, Second Edition*. CRC Press, Taylor & Francis Group, Boca Raton, FL.
- Nanjaiah, M., Pilipodi-Best, A., Lalanne, M., Fjodorow, P., Schulz, C., Cheskis, S., Kempf, A., Wlokas, I., & Rahinov, I. (2020). Experimental and numerical investigation of iron-doped flames: FeO formation and impact on flame temperature. *Proceedings of the Combustion Institute*. <https://doi.org/10.1016/j.proci.2020.07.006>
- Noll, K. E., & Pilat, M. J. (1970). Inertial impaction of particles upon rectangular bodies. *Journal of Colloid and Interface Science*, 33(2), 197–207. [https://doi.org/10.1016/0021-9797\(70\)90022-6](https://doi.org/10.1016/0021-9797(70)90022-6)
- Ochiai, A., Imoto, J., Suetake, M., Komiya, T., Furuki, G., Ikehara, R., Yamasaki, S., Law, G. T. W., Ohnuki, T., Grambow, B., Ewing, R. C., & Utsunomiya, S. (2018). Uranium Dioxides and Debris Fragments Released to the Environment with Cesium-Rich Microparticles from the Fukushima Daiichi Nuclear Power Plant. *Environmental Science & Technology*, 52(5), 2586–2594. <https://doi.org/10.1021/acs.est.7b06309>
- Ouyang, H., Gopalakrishnan, R., & Hogan, C. J. (2012). Nanoparticle collisions in the gas phase in the presence of singular contact potentials. *The Journal of Chemical Physics*, 137(6), 064316. <https://doi.org/10.1063/1.4742064>
- Oxtoby, D. W. (1992). Homogeneous nucleation: Theory and experiment. *Journal of Physics: Condensed Matter*, 4(38), 7627–7650. <https://doi.org/10.1088/0953-8984/4/38/001>
- Pope, C. J., & Howard, J. B. (1997). Simultaneous Particle and Molecule Modeling (SPAMM): An Approach for Combining Sectional Aerosol Equations and Elementary Gas-Phase Reactions. *Aerosol Science and Technology*, 27(1), 73–94. <https://doi.org/10.1080/02786829708965459>
- S. Glasstone and P. J. Dolan. (1977). *The Effects of Nuclear Weapons, 3rd Edition, US Department of Defense and US Department of Energy*.
- Savel'ev, A. M., & Starik, A. M. (2017). An improved model of homogeneous nucleation for high supersaturation conditions: Aluminum vapor. *Physical Chemistry Chemical Physics*, 19(1), 523–538. <https://doi.org/10.1039/C6CP04080B>

- Savel'ev, A. M., & Starik, A. M. (2018). The formation of $(\text{Al}_2\text{O}_3)_n$ clusters as a probable mechanism of aluminum oxide nucleation during the combustion of aluminized fuels: Numerical analysis. *Combustion and Flame*, *196*, 223–236. <https://doi.org/10.1016/j.combustflame.2018.06.017>
- Sceats, M. G. (1989). Brownian coagulation in aerosols—The role of long range forces. *Journal of Colloid and Interface Science*, *129*(1), 105–112. [https://doi.org/10.1016/0021-9797\(89\)90419-0](https://doi.org/10.1016/0021-9797(89)90419-0)
- Sharipov A. S., Loukhovitski B. I., & Starik A. M. (2013). Theoretical Study of Structure and Physical Properties of $(\text{Al}_2\text{O}_3)_n$ Clusters. *Phys. Scr.*, *88*, 058307.
- Shin, J. W., Miyazoe, H., Leparoux, M., Siegmann, S., Dorier, J. L., & Hollenstein, C. (2006). *The influence of process parameters on precursor evaporation for alumina nanopowder synthesis in an inductively coupled rf thermal plasma*. *15*, 441–449.
- Sitarski, M., & Nowakowski, B. (1979). Condensation rate of trace vapor on Knudsen aerosols from the solution of the Boltzmann equation. *Journal of Colloid and Interface Science*, *72*(1), 113–122. [https://doi.org/10.1016/0021-9797\(79\)90187-5](https://doi.org/10.1016/0021-9797(79)90187-5)
- Smirnov, V. N. (2012). Thermochemical parameters and rate constants of the reactions $\text{Fe} + \text{O}_2 + \text{MA} \leftrightarrow \text{FeO}_2 + \text{M}$ and $\text{FeO} + \text{O}_2 \leftrightarrow \text{FeO}_2 + \text{O}$. *Kinetics and Catalysis*, *53*, 543–553.
- Starik, A. M., Savel'ev, A. M., & Titova, N. S. (2015). Specific features of ignition and combustion of composite fuels containing aluminum nanoparticles (Review). *Combustion, Explosion, and Shock Waves*, *51*(2), 197–222. <https://doi.org/10.1134/S0010508215020057>
- Yamamuro, S., Sumiyama, K., & Suzuki, K. (1999). Monodispersed Cr cluster formation by plasma-gas-condensation. *Journal of Applied Physics*, *85*(1), 483–489.

Supplementary Information

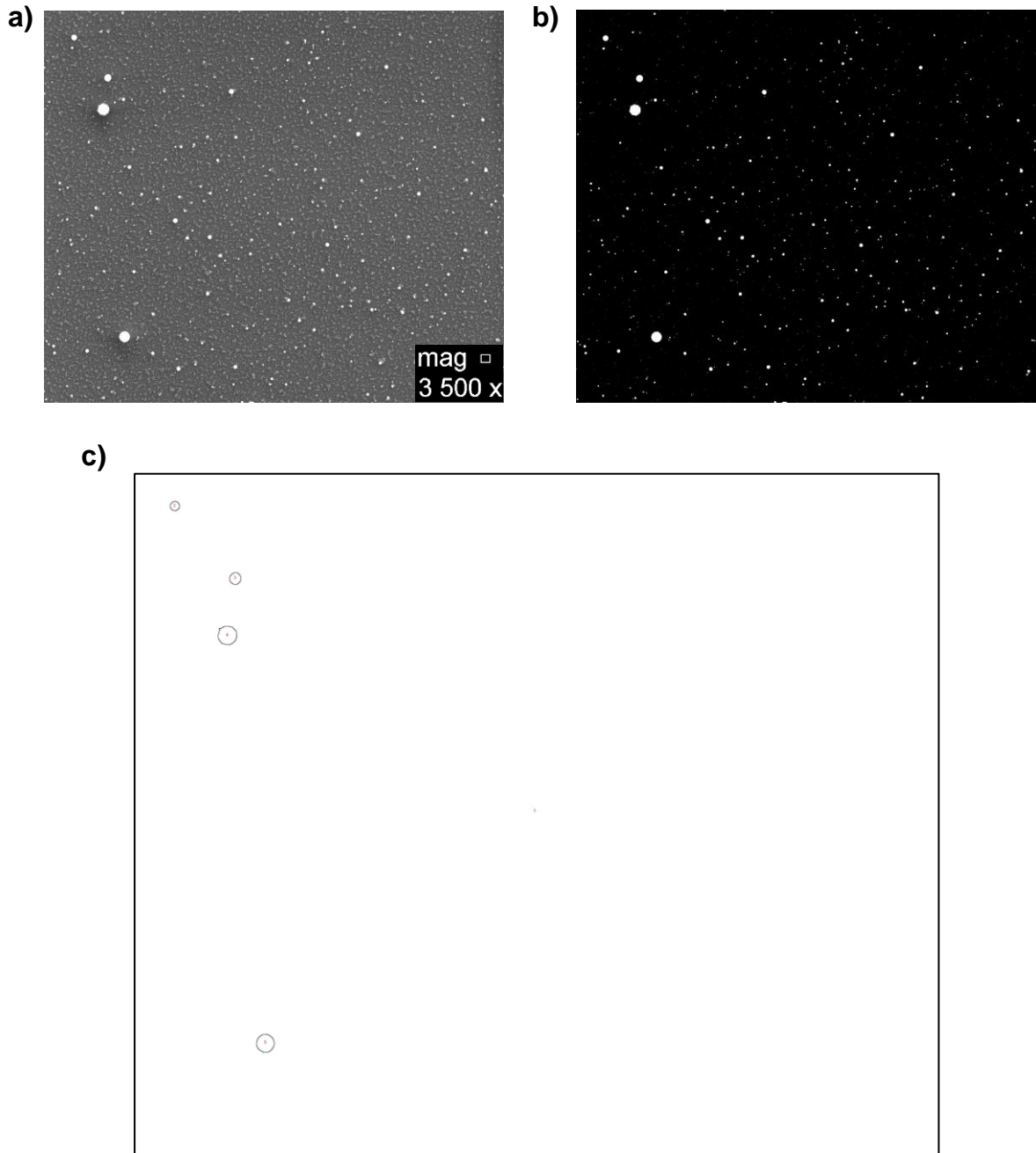


Figure S - 1 The SEM image of aluminum oxide particles shown in (a) is taken at 3500 magnification. The image is converted to a binary image and displayed in (b). The binary image is used to detect the edges of the particles. The particles of sizes greater than 600 nm are shown in (c).

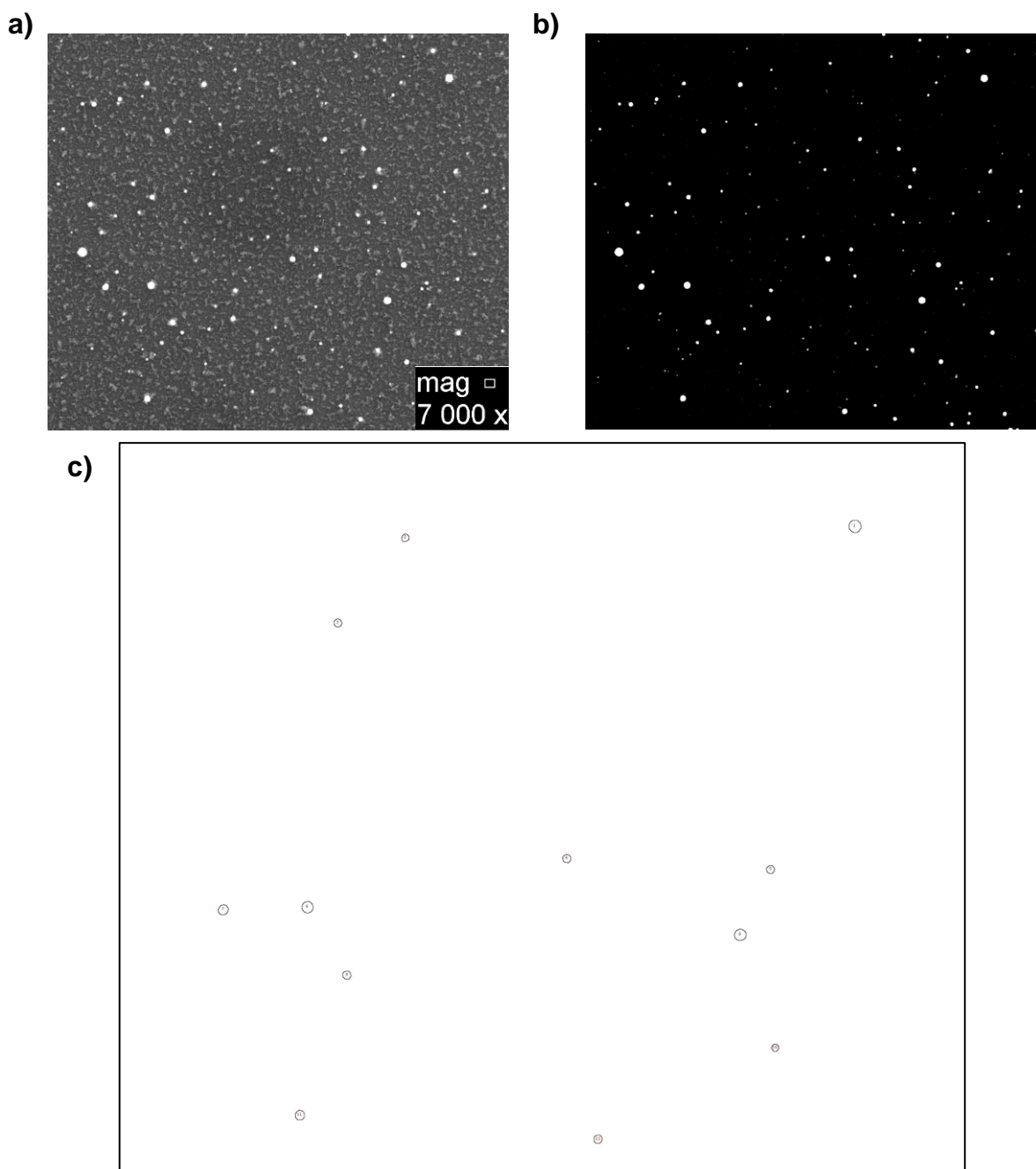


Figure S - 2 The SEM image of aluminum oxide particles shown in (a) is taken at 7000 magnification. The image is converted to a binary image and displayed in (b). The binary image is used to detect the edges of the particles. The particles of sizes between 300 nm and 600 nm are shown in (c).